

Crystal Structure of the Vanadate-Inhibited Ca²⁺-ATPase

Johannes D. Clausen^{1,2,3,5,7}, Maike Bublitz^{1,2,6,7}, Bertrand Arnou^{1,2}, Claus Olesen^{1,2,3}, Jens Peter Andersen³, Jesper Vuust Møller^{2,3}, and Poul Nissen^{1,2,4,*}

¹Department of Molecular Biology and Genetics, Aarhus University, 8000 Aarhus C, Denmark

²Centre for Membrane Pumps in Cells and Disease – PUMPKIN, Danish National Research Foundation, Aarhus University, 8000 Aarhus C, Denmark

³Department of Biomedicine, Aarhus University, 8000 Aarhus C, Denmark

⁴Danish Research Institute of Translational Neuroscience – DANDRITE, Nordic EMBL Partnership for Molecular Medicine, Aarhus University, 8000 Aarhus C, Denmark

⁵Present address: Pcovery ApS, Ole Maaløes Vej 3, 2200 Copenhagen N, Denmark.

⁶Present address: Department of Biochemistry, University of Oxford, Oxford OX1 3QU, United Kingdom

⁷These authors contributed equally to this work.

*Correspondence: pn@mbg.au.dk

SUMMARY

Vanadate is the hallmark inhibitor of the P-type ATPase family; however, structural details of its inhibitory mechanism have remained unresolved. We have determined the crystal structure of sarcoplasmic reticulum Ca^{2+} -ATPase with bound vanadate in the absence of Ca^{2+} . Vanadate is bound at the catalytic site as a planar VO_3^- in complex with water and Mg^{2+} in a dephosphorylation transition state-like conformation. Validating bound VO_3^- by anomalous difference Fourier maps using long wavelength data we also identify a hitherto undescribed Cl^- site near the dephosphorylation site. Crystallization was facilitated by trinitrophenyl (TNP)-derivatized nucleotides that bind with the TNP-moiety occupying the binding pocket that normally accommodates the adenine of ATP, rationalizing their remarkably high affinity for *E2P*-like conformations of the Ca^{2+} -ATPase. A comparison of the configurations of bound nucleotide analogs in the *E2*· VO_3^- structure with that in *E2*· BeF_3^- (*E2P* ground state analog) reveals multiple binding modes to the Ca^{2+} -ATPase.

INTRODUCTION

Vanadate is a potent inhibitor of a large variety of enzymes that interact with phosphate compounds, including also the P-type ATPases (Cantley et al., 1978; Dupont and Bennett, 1982; Pick, 1982). Models of the inhibitory mechanism of vanadate are generally based on its structural and chemical similarity to phosphate, and the ability of vanadate to adopt a pentacoordinated trigonal bipyramidal geometry analogous to the transition state for phosphate ester hydrolysis of phosphoryl transfer (Crans et al., 2004; Davies and Hol, 2004). However, vanadate solutions typically exist as a complex mixture of the monomeric orthovanadate ion and various oligomeric species that also bind with high affinity to P-type ATPases and inhibit their activity (Aureliano, 2000; Csermely et al., 1985a), giving rise to some confusion about the actual chemical nature of vanadate inhibition.

Decameric vanadate, favored at low pH, likely asserts its inhibitory effect by competing with ATP for binding (Coan et al., 1986; Csermely et al., 1985b; Hua et al., 2000).

Previous X-ray crystallographic studies of *E2P*-like conformations of P-type ATPases have employed aluminum fluoride (AlF_4^-), magnesium fluoride (MgF_x), or beryllium fluoride (BeF_3^-) as phosphate analogs (Gourdon et al., 2011; Morth et al., 2007; Olesen et al., 2007; Olesen et al., 2004; Toyoshima et al., 2004) (**Figure 1A**), however, neither of these are isosteric with the trigonal bipyramidal transition state of a phosphoryl transfer reaction. AlF_4^- adopts a square planar geometry (Sorensen et al., 2004b), whereas MgF_x and BeF_3^- are non-planar and rather mimic a tetrahedral phosphate anion and a phosphorylated state, respectively (Olesen et al., 2007; Toyoshima et al., 2004). Vanadate is therefore thought to mimic the phosphoryl transition state more accurately than the metal-fluoride compounds (Davies and Hol, 2004). To obtain structural insight into the phosphoryl transfer reaction during the autophosphatase activity of the Ca^{2+} -ATPase (**Figure 1A**), and to clarify the differential effects of vanadate inhibition of transport activity, we have determined the structure of the vanadate-inhibited Ca^{2+} -ATPase.

RESULTS AND DISCUSSION

Vanadate Stabilizes the Ca^{2+} -ATPase in an *E2·P* Transition State-Like Conformation

Ca^{2+} -ATPase, pre-equilibrated with orthovanadate (VO_4^{3-}) and Mg^{2+} (a critical co-factor for orthovanadate binding (Dupont and Bennett, 1982)) in the absence of Ca^{2+} to accumulate the orthovanadate-reactive *E2* form (Pick, 1982), was crystallized and analyzed by X-ray diffraction (**Figure S1 and Table S1**). Crystals grown in the presence of 2',3'-*O*-(2,4,6-trinitrophenyl)- β , γ -methyleneadenosine 5'-triphosphate (TNP-AMPPCP) and the Ca^{2+} -ATPase-specific membrane-bound inhibitor thapsigargin diffracted to 3.05 Å resolution, and data were collected at a wavelength of

either 0.98 or 2.21 Å, both of which provide a significant anomalous signal for vanadium ($f''_{0.98 \text{ Å}} = 1.0$ e; $f''_{2.21 \text{ Å}} = 3.8$ e).

The $E2 \cdot VO_3^- \cdot \text{thapsigargin} \cdot \text{TNP-AMPPCP}$ structure (**Figure 1B**) was determined by molecular replacement using the structure of the $E2 \cdot AlF_4^- \cdot \text{thapsigargin}$ form of the Ca^{2+} -ATPase (Olesen et al., 2004) as search model. Two strong electron density peaks of 20.8 and 9.5 σ , respectively, were present at the catalytic site in an unbiased $mF_o - DF_c$ omit map (*green mesh* in **Figure 2A**). A dimeric vanadate model (*i.e.* pyrovanadate) was excluded by anomalous difference Fourier map analysis (*orange mesh* in **Figure 2A**), showing only anomalous scattering from one of the two density peaks (peak height 19.3 σ , background maximum of 4.2 σ for highest negative peak). Hence, vanadate binds at the catalytic site as orthovanadate, which exhibits preferential binding to $E2$ (Cantley et al., 1978; Dupont and Bennett, 1982; Pick, 1982) (**Figure S2A**), even though oligo-vanadate forms are likely present in exceeding amounts under the experimental conditions (see legend to **Figure S2**). The $mF_o - DF_c$ density peak at the catalytic site was well accounted for by a planar VO_3^- in a trigonal bipyramidal phosphate transition state-like conformation, as expected for an associative transfer mechanism (Davies and Hol, 2004), flanked by a Mg^{2+} ion and three water molecules in positions similar to those seen in the $E2 \cdot AlF_4^-$ structure (Bublitz et al., 2013; Olesen et al., 2004) (**Figure 2B**).

The VO_3^- is coordinated between Asp³⁵¹, the residue that is phosphorylated by ATP, and a water molecule held in place by the carboxyl side chain of Glu¹⁸³, the main chain carbonyl of Thr¹⁸¹ (both of the general P-type ATPase autophosphatase motif TGE) and the main chain nitrogen of Gly⁶²⁶ (**Figure 2A**). Indeed, mutations of Thr¹⁸¹ and Glu¹⁸³ are strongly detrimental to orthovanadate binding (Anthonisen et al., 2006). The catalytic Mg^{2+} ion displays octahedral coordination geometry, with coordination provided by a VO_3^- oxygen, the side chain carboxyls of Asp³⁵¹ and Asp⁷⁰³, the main chain oxygen of Thr³⁵³, and two water molecules (**Figure 2A**).

Like vanadate, AlF_4^- is thought to stabilize an $E2 \cdot P$ transition state-like conformation of the Ca^{2+} -ATPase (Olesen et al., 2007; Olesen et al., 2004). Overall, the structure of $E2 \cdot VO_3^-$ varies very little from that of $E2 \cdot AlF_4^-$, suggesting that they both represent the same, close mimic of a true

dephosphorylation intermediate. Alignment of the catalytic sites of $E2\cdot VO_3^-$ and $E2\cdot AlF_4^-$ shows that the arrangement of the critical side chains is roughly superposable in the two structures, as are the positions of the water molecules and the Mg^{2+} ion (**Figure 2B**). The vanadium atom and two of the oxygens of VO_3^- overlap well with the aluminum atom and two of the fluorine atoms of AlF_4^- , respectively. The third VO_3^- oxygen is positioned roughly halfway between the remaining two AlF_4^- fluorine atoms. In $E2\cdot AlF_4^-$, these two fluorine atoms are hydrogen bonded to the main chain nitrogen of Gly⁶²⁶ and the side chain amide of Asn⁷⁰⁶ at ca. 2.5 Å and 2.7 Å distance, respectively, whereas in $E2\cdot VO_3^-$ similar interactions with the corresponding VO_3^- oxygen are of ca. 2.8 and 3.4 Å distance, respectively.

The catalytic domain of the P-type ATPases shares ancestry and structural homology with members of the haloacid dehalogenase superfamily of phosphotransferases (Aravind et al., 1998). **Figure 2C** shows an alignment of the catalytic site in $E2\cdot VO_3^-$ with that of the vanadate complex of the hexose phosphate transferase, which has been determined at 1.0 Å resolution (Lu et al., 2008), illustrating the high homology of the catalytic site in the phosphoryl transfer transition states of the two enzymes and also validating our model.

Decavanadate Inhibits the Ca^{2+} -ATPase by Competing with Nucleotide for Binding

Previous analyses (Coan et al., 1986; Csermely et al., 1985b; Hua et al., 2000) have shown that oligomeric vanadate species can bind to a site in the Ca^{2+} -ATPase distinct from the phosphorylation site. In accordance with this view we show here (**Figures S2B and C**) that decavanadate, but not orthovanadate, competes with the binding of TNP-8N₃-ATP, whose binding site in the Ca^{2+} -ATPase overlaps with that of ATP (McIntosh et al., 1992). Indeed, the affinity of the nucleotide site for decavanadate is remarkably high in both the Ca_2E1 and $E2\cdot VO_3^-$ states, displaying K_D values of 2.7 and 15 nM, respectively (**Figure S2**). In contrast, the binding and inhibition by orthovanadate occurs exclusively in the $E2$ state (Dupont and Bennett, 1982; Pick, 1982) (**Figure S2**). The idea that decavanadate preferentially binds to the nucleotide site furthermore agrees with the previous

suggestion (Hua et al., 2000; Toyoshima et al., 2000; Stokes et al., 2005) that a particular area of electron density, seen in the groove between the N- and P-domains of the Ca^{2+} -ATPase in low-resolution (8 Å) electron density maps obtained by cryoelectron microscopy of tubular crystals (Zhang et al., 1998; Stokes et al., 2005), corresponds to decavanadate.

A Chloride Binding Site in the $E2\cdot\text{VO}_3^-$ Structure

We identify a hitherto undescribed chloride binding site in the P-domain of the $E2\cdot\text{VO}_3^-$ structure near conserved residues Asn⁶²⁸ and Arg⁶⁷⁸ (**Figure 1B and Figure 3**). The ligand at the site was assigned as a chloride ion on the basis of an anomalous difference Fourier peak of 6.0 σ (**Figure 3A**), thus excluding water as a possibility, combined with the buffer composition during crystallization, which included, as the only anion present in appreciable amounts, 45-70 mM Cl^- . Interestingly, all the previously published $E2\cdot\text{AlF}_4^-$ and $E2\cdot\text{MgF}_x$ structures with deposited structure factors in the PDB database (three structures for $E2\cdot\text{AlF}_4^-$ and four for $E2\cdot\text{MgF}_x$) also display a spherical electron density peak at a position overlapping with the chloride site in $E2\cdot\text{VO}_3^-$ (Bublitz et al., 2013; Laursen et al., 2009; Moncoq et al., 2007; Olesen et al., 2007; Toyoshima et al., 2011), as does a 2.4 Å $E2\cdot\text{MgF}_x$ structure of the closely related Na^+, K^+ -ATPase (Shinoda et al., 2009). In these structures, the density has been assigned as water or, in two cases, been left unassigned.

Given the close proximity of the chloride site in $E2\cdot\text{VO}_3^-$ to the catalytic site (**Figure 3C**) it is tempting to speculate, that the site could stabilize the $E2\cdot\text{P}$ dephosphorylation transition state, reminiscent of the role played by K^+ in mediating contacts between the P-domain and the transmembrane region (Sorensen et al., 2004a) (**Figure 1B**), a structural element critical for the stimulation of dephosphorylation (Shigekawa and Pearl, 1976). Asn⁶²⁸ is connected via the protein backbone to the highly conserved ⁶²⁵TGD motif, a critical element for both phosphorylation and nucleotide binding (McIntosh et al., 2004), which in turn is connected to the dephosphorylation site in $E2\cdot\text{VO}_3^-$ via direct interactions with the attacking water (**Figure 3C**). Furthermore, the Cl^- site is closely connected to the nucleotide site via the interactions of Arg⁶⁷⁸ and Asn⁶²⁸ with the Mg^{2+} -

phosphate moiety of TNP-AMPPCP (**Figure 3C**), suggesting that Cl^- binding could be an important factor for the well-known stimulatory effect of ATP on the rate of *E2P* dephosphorylation (Clausen et al, 2011; Shigekawa and Dougherty, 1978).

TNP-nucleotides Bind with the TNP-Moiety Occupying the Binding Pocket that Normally Accommodates the Adenine of ATP

Co-crystallization with a TNP-derivatized nucleotide was a prerequisite for the formation of diffraction-quality crystals of the *E2*· VO_3^- form (**Figure S1**), perhaps as a necessity to yield a homogenous sample in a poly-vanadate background. TNP-nucleotides are widely used as probes for the P-type ATPases, owing to their fluorescent properties and their high affinity for these enzymes, and have found application in a wide range of biochemical assays for the study of P-type ATPase function (McIntosh, 1998). Thus, TNP-derivatized nucleotides bind to the *E2P* conformations of the Ca^{2+} -ATPase with affinities that are 2-3 orders of magnitude higher than those of the parent nucleotides (**Table 1 and Figure S3**). The high quality of the electron density maps allowed us to unambiguously place the TNP-AMPPCP into the *E2*· VO_3^- structural model (**Figure 4A and Figure S4, A-C**), further confirmed by anomalous signals for the α -, β -, and γ - phosphates (peaks in the anomalous difference Fourier map of 2.9, 3.0, and 5.6 σ , respectively). Interestingly, the TNP moiety of TNP-AMPPCP (or TNP-ATP, which we find is bound similarly to TNP-AMPPCP) is located in the binding pocket that normally accommodates the adenine moiety of AMPPCP/ATP (Olesen et al., 2007; Toyoshima et al., 2011), surrounded by the side chains of Arg¹⁷⁴, Glu⁴³⁹, Thr⁴⁴¹, Glu⁴⁴², Phe⁴⁸⁷, Lys⁵¹⁵, and Leu⁵⁶². The adenine instead is stacked between Val¹⁸⁵ and Arg⁵⁶⁰, and the triphosphate moiety is held in place by the side chains of Lys²⁰⁵, Arg⁵⁶⁰, and Arg⁶⁷⁸, and a Mg^{2+} ion coordinated by the side chain oxygen of Asn⁶²⁸. Despite the different binding mode, the overall arrangement of side chains forming the binding site for TNP-AMPPCP in *E2*· VO_3^- is remarkably similar to that seen in the *E2*· AlF_4^- ·AMPPCP structure (Olesen et al., 2007) (**Figure S4, D-E**), with a 3-4 Å shift of Arg⁵⁶⁰ as the only major difference to accommodate the adenine. Hence, the TNP-nucleotides fit readily into the

naturally preformed nucleotide binding pocket of the *E2P* transition state of dephosphorylation, albeit with an extra element (the TNP) contributing to binding, explaining their unusually high binding affinity (**Table 1**).

TNP-Nucleotides Display a Dual Binding Mode in the *E2P*-Like Conformations of the Ca^{2+} -ATPase

For further comparison, we also produced crystals of the Ca^{2+} -ATPase in the $E2\cdot\text{BeF}_3^-$ state (*E2P* ground state analog, see **Figure 1A**) co-crystallized with TNP-AMPPCP. The structure was determined at 3.05 Å resolution (**Table S1**) by molecular replacement using the previously published nucleotide-free $E2\cdot\text{BeF}_3^-$ structure (Olesen et al., 2007) as search model. The refinement unambiguously reveals the orientation of the nucleotide in this *E2P*-like structure (**Figure 4B**): the TNP moiety occupies the same binding pocket as in $E2\cdot\text{VO}_3^-$, however the remainder of the nucleotide displays markedly different interactions (compare **Figures 4A and 4B**). Hence, relative to the binding configuration seen in the $E2\cdot\text{VO}_3^-$ structure, the entire nucleotide in $E2\cdot\text{BeF}_3^-$ is rotated by $\sim 180^\circ$ around an axis along the plane of the TNP, such that the 2',3'-oxygen of the ribose, that connect to the TNP, extend in the opposite direction. Consequently, the adenine and phosphate moieties likewise extend in opposite directions relative to those seen in the $E2\cdot\text{VO}_3^-$ structure. The overall outcome is a strikingly different mode of TNP-AMPPCP binding in $E2\cdot\text{BeF}_3^-$. A similar binding mode in $E2\cdot\text{BeF}_3^-$ was found previously for TNP-AMP (Toyoshima et al., 2011), although with the ribose and adenine moieties somewhat displaced (by up to 4 Å) relative to the configuration seen in our $E2\cdot\text{BeF}_3^-$ structure, possibly owing to the absence of the β - and γ - phosphates. **Figure S4F** compares the position of the adenine moiety of TNP-AMPPCP in $E2\cdot\text{BeF}_3^-$ and $E2\cdot\text{VO}_3^-$ with that of AMPPCP in $E2\cdot\text{AlF}_4^-$ -AMPPCP (Olesen et al., 2007), illustrating the high degree of variability with respect to its position in these three structures. The different binding configurations of the adenine moiety may delineate intermediate sites and pathways of nucleotide entry/exit to and from the binding site during ADP/ATP exchange.

The different structural arrangements of the nucleotide binding pocket in $E2\cdot\text{BeF}_3^-$ ($E2P$ ground state analog) and $E2\cdot\text{VO}_3^-$ ($E2\cdot P$ transition state analog) mirrors the variation in nucleotide affinity between the two reaction states, the affinity being invariably higher in the transition state conformation than in the ground state conformation (**Table 1**). This reflects the well-known stimulating effect of ATP on the rate of $E2P$ dephosphorylation (Clausen et al., 2011; Shigekawa and Dougherty, 1978). Furthermore, the two different TNP-nucleotide binding modes rationalize the previous finding (Clausen et al., 2011), that the efficiency of photolabeling of Lys⁴⁹² by the 8-azido derivative of TNP-ATP (TNP-8N₃-ATP) (McIntosh et al., 1992) varies markedly between different intermediate reaction states in the Ca^{2+} -ATPase reaction cycle (**Figure 1A**). The labeling stoichiometry in $E2\cdot\text{BeF}_3^-$, $E2\cdot\text{AlF}_4^-$, $E2\cdot\text{VO}_3^-$, $E2\cdot\text{MgF}_x$, $E2$, and $E1$ ranges from 0.2 to 0.7 mol of label incorporated per mol of Ca^{2+} -ATPase present (Clausen et al., 2011), likely reflecting a varying partitioning for the individual reaction states between the two different TNP-nucleotide binding modes. Hence, only the nucleotide binding configuration corresponding to **Figure 4B** would be compatible with labeling, whereas in the configuration corresponding to **Figure 4A** the 8-position of the adenine is too distant from Lys⁴⁹² for labeling to be feasible.

Conclusion

This first crystal structure of a vanadate-inhibited P-type ATPase, in combination with direct binding studies, allows us to define the molecular details of orthovanadate-inhibition, and to reveal a markedly distinct effect of decavanadate. Whereas the former acts as an isosteric trigonal planar phosphoryl transfer mimic, the latter competes with nucleotide binding. Our study further reveals a previously undescribed Cl^- binding site near the catalytic site that may play a structural role in stabilization of the dephosphorylation transition state. We find an unexpected dual binding mode for TNP-derivatized nucleotides to the $E2P$ -like conformations of the Ca^{2+} -ATPase, rationalizing why labeling efficiency with TNP-8N₃-ATP depends on the functional state of the enzyme and hinting at

flexible binding modes for nucleotides to exchange at the catalytic site. Altogether, our studies provide important new details for accurate modeling of SERCA dynamics and function.

EXPERIMENTAL PROCEDURES

Nucleotide Synthesis

TNP-ATP, TNP-AMPPCP, TNP-ADP, and TNP-8N₃-ATP were prepared similarly, by TNP-derivatization of the parent nucleotides, as detailed in Supplemental Experimental Procedures.

Preparation of Vanadate Solutions

Stock solutions enriched in either orthovanadate or decavanadate were prepared according to previously established protocols (see Supplemental Experimental Procedures).

Protein Preparation

Sarcoplasmic reticulum Ca²⁺-ATPase (SERCA1a isoform) for crystallization trials and biochemical experiments was prepared from sarcoplasmic reticulum vesicles isolated from rabbit hind leg skeletal muscle according to established procedures (Andersen et al., 1985). The membranes were washed by centrifugation and the Ca²⁺-ATPase accumulated in the *E*2·VO₃⁻ and *E*2·BeF₃⁻ states by incubation of the membrane preparations with orthovanadate or BeSO₄ and NaF and either with or without thapsigargin and nucleotide, as under the conditions detailed in Supplemental Experimental Procedures.

Protein Crystallization

Crystallization was carried out using the vapor diffusion technique in hanging crystallization drops, as described in Supplemental Experimental Procedures. The crystallization buffers that gave rise to the

crystals, from which the highest resolution X-ray diffraction data sets were obtained, are detailed in **Table S1**. The crystals were mounted in either LithoLoops (Molecular Dimensions) or nylon CryoLoops (Hampton Research) before flash-cooling in liquid nitrogen.

Diffraction Data Collection and Structure Refinement

The synchrotron facilities at which the X-ray diffraction data were collected are listed in Supplemental Experimental Procedures. The data were processed and scaled using the XDS package (Kabsch, 1993), and structure determination by molecular replacement was carried out with *PHASER*, using the *PHENIX AutoMR* function (Adams et al., 2010; McCoy et al., 2007). Unbiased difference Fourier maps (simulated annealing omit maps) and anomalous difference Fourier maps were calculated with PHENIX or with programs from the CCP4 suite (Read, 1990; Read and Schierbeek, 1988; Winn et al., 2011). The models were built in Coot (Emsley et al., 2010) and refinement was performed with PHENIX (Adams et al., 2010). B-factor distributions were calculated using data from the PDB (www.rcsb.org/pdb) and MemProtMD (Stansfield et al., 2015) databases.

Competitive Inhibition of [γ - ^{32}P]TNP-8N₃-ATP Photolabeling

The synthesis of the [γ - ^{32}P]TNP-8N₃-ATP photolabel, its application as a specific photolabel of the Ca²⁺-ATPase, the competitive inhibition by various ligands (nucleotides and monomeric/polymeric vanadate species) of [γ - ^{32}P]TNP-8N₃-ATP photolabeling, the quantification of ^{32}P -labeled bands by electronic autoradiography following SDS-PAGE, and the analysis of the results were carried out using previously established procedures, as detailed in Supplemental Experimental Procedures.

Analysis of Functional Data and Statistics

The functional experiments were conducted at least twice, and average values with standard errors are shown in the figures. The complete data sets (including all experimental data points before averaging) were analyzed by nonlinear regression using the SigmaPlot program (Systat Software

Inc.), giving the lines in the figures and the affinity constants and S.E. listed in the figure legends and tables. The equations used and the total number of data points included in the fits, as well as the number of independent experiments (n), are detailed in the figure legends and tables.

ACCESSION NUMBERS

Atomic coordinates and structure factors for the 3.05 Å *E2*·VO₃⁻·thapsigargin·TNP-AMPPCP, the 3.05 Å *E2*·BeF₃⁻·TNP-AMPPCP, and the 3.30 Å *E2*·VO₃⁻·thapsigargin·TNP-ATP structures have been deposited in the Protein Data Bank under accession codes 5A3Q, 5A3R, and 5A3S, respectively.

SUPPLEMENTAL INFORMATION

Supplemental Information includes four figures, one table, Supplemental Experimental Procedures, and Supplemental References and can be found with this article online at <http://xxxx>.

ACKNOWLEDGEMENTS

We thank Birthe Nielsen, Lisbeth Nielsen, Lene Jacobsen, and Karin Kracht (Department of Biomedicine, Aarhus University, Denmark) and Jesper L. Karlsen and Anna Marie Nielsen (Department of Molecular Biology and Genetics, Aarhus University, Denmark) for expert technical assistance. Beam time and support at the Deutsches Elektronen-Synchrotron DESY (Hamburg, Germany), the Swiss Light Source (Villigen, Switzerland), the SOLEIL Synchrotron (Gif-sur-Yvette Cedex, France), the European Synchrotron Radiation Facility (Grenoble, France), the Diamond Light Source (Oxfordshire, UK), and the MAX Laboratory (Lund, Sweden) are greatly acknowledged. We are grateful to Dr. Thomas Boesen, Dr. Linda Reinhard, Dr. Mette Laursen, Dr. Joseph Lyons, Dr. Pontus Gourdon, and Dr. Jonas L. Gregersen for help with synchrotron data collection. We thank

Ariane Sahebzade, Goethe-University Frankfurt, for help with model building and refinement and Thomas Newport and Dr. Phillip J. Stansfeld, University of Oxford, for help with B-factor comparisons. This work was supported by grants from the Lundbeck Foundation (to J.D.C. and P.N.), the Danish Medical Research Council (to J.P.A.), the Novo Nordisk/Vilhelm Pedersen Foundation (to J.P.A. and J.V.M), and the Danish Council for Strategic Research (to M.B., J.V.M., and P.N.).

AUTHOR CONTRIBUTIONS

J.D.C. and B.A. initiated the project. C.O. and J.V.M. prepared sarcoplasmic reticulum membranes. J.D.C. synthesized TNP-derivatized nucleotides. J.D.C., B.A., and M.B. crystallized the protein. J.D.C., M.B., B.A., and C.O. collected and processed the X-ray diffraction data. M.B., J.D.C., and B.A. refined the structural models. J.D.C. carried out the biochemical analysis. J.D.C. wrote the paper with M.B., J.P.A., and P.N. and with comments from all authors.

COMPETING FINANCIAL INTERESTS

The authors declare no competing financial interests.

REFERENCES

- Adams, P.D., Afonine, P.V., Bunkoczi, G., Chen, V.B., Davis, I.W., Echols, N., Headd, J.J., Hung, L.W., Kapral, G.J., Grosse-Kunstleve, R.W., *et al.* (2010). PHENIX: a comprehensive Python-based system for macromolecular structure solution. *Acta Crystallogr. D Biol. Crystallogr.* 66, 213-221.
- Andersen, J.P., Lassen, K., and Moller, J.V. (1985). Changes in Ca²⁺ affinity related to conformational transitions in the phosphorylated state of soluble monomeric Ca²⁺-ATPase from sarcoplasmic reticulum. *J. Biol. Chem.* 260, 371-380.

1 Anthonisen, A.N., Clausen, J.D., and Andersen, J.P. (2006). Mutational analysis of the conserved TGES loop of
2 sarcoplasmic reticulum Ca²⁺-ATPase. *J. Biol. Chem.* *281*, 31572-31582.
3
4 Aravind, L., Galperin, M.Y., and Koonin, E.V. (1998) The catalytic domain of the P-type ATPase has the haloacid
5 dehalogenase fold. *Trends Biochem. Sci.* *23*, 127-129.
6
7 Aureliano, M. (2000). Vanadate oligomer inhibition of passive and active Ca²⁺ translocation by the Ca²⁺ pump
8 of sarcoplasmic reticulum. *J. Inorg. Biochem.* *80*, 145-147.
9
10 Bublitz, M., Musgaard, M., Poulsen, H., Thogersen, L., Olesen, C., Schiott, B., Morth, J.P., Moller, J.V., and
11 Nissen, P. (2013). Ion Pathways in the Sarcoplasmic Reticulum Ca²⁺-ATPase. *J. Biol. Chem.* *288*, 10759-
12 10765.
13
14 Cantley, L.C., Jr., Cantley, L.G., and Josephson, L. (1978). A characterization of vanadate interactions with the
15 (Na,K)-ATPase. Mechanistic and regulatory implications. *J. Biol. Chem.* *253*, 7361-7368.
16
17 Clausen, J.D., McIntosh, D.B., Woolley, D.G., and Andersen, J.P. (2011). Modulatory ATP binding affinity in
18 intermediate states of E2P dephosphorylation of sarcoplasmic reticulum Ca²⁺-ATPase. *J. Biol. Chem.* *286*,
19 11792-11802.
20
21 Coan, C., Scales, D.J., and Murphy, A.J. (1986). Oligovanadate binding to sarcoplasmic reticulum ATPase.
22 Evidence for substrate analogue behavior. *J. Biol. Chem.* *261*, 10394-10403.
23
24 Crans, D.C., Smee, J.J., Gaidamauskas, E., and Yang, L. (2004). The chemistry and biochemistry of vanadium and
25 the biological activities exerted by vanadium compounds. *Chem. Rev.* *104*, 849-902.
26
27 Csermely, P., Martonosi, A., Levy, G.C., and Ejchart, A.J. (1985a). 51V-n.m.r. analysis of the binding of
28 vanadium(V) oligoanions to sarcoplasmic reticulum. *Biochem. J.* *230*, 807-815.
29
30 Csermely, P., Varga, S., and Martonosi, A. (1985b). Competition between decavanadate and fluorescein
31 isothiocyanate on the Ca²⁺-ATPase of sarcoplasmic reticulum. *Eur. J. Biochem.* *150*, 455-460.
32
33 Danko, S., Yamasaki, K., Daiho, T., and Suzuki, H. (2004). distinct natures of beryllium fluoride-bound,
34 aluminum fluoride-bound, and magnesium fluoride-bound stable analogues of an ADP-insensitive
35 phosphoenzyme intermediate of sarcoplasmic reticulum Ca²⁺-ATPase: changes in catalytic and transport
36 sites during phosphoenzyme hydrolysis. *J. Biol. Chem.* *279*, 14991-14998.
37
38 Davies, D.R., and Hol, W.G. (2004). The power of vanadate in crystallographic investigations of phosphoryl
39 transfer enzymes. *FEBS Lett.* *577*, 315-321.
40
41
42
43
44
45
46
47
48
49
50
51
52
53
54
55
56
57
58
59
60
61
62
63
64
65

Dupont, Y., and Bennett, N. (1982). Vanadate inhibition of the Ca^{2+} -dependent conformational change of the sarcoplasmic reticulum Ca^{2+} -ATPase. *FEBS Lett.* 139, 237-240.

Emsley, P., Lohkamp, B., Scott, W.G., and Cowtan, K. (2010). Features and development of Coot. *Acta Crystallogr. D Biol. Crystallogr.* 66, 486-501.

Gourdon, P., Liu, X.Y., Skjorring, T., Morth, J.P., Moller, L.B., Pedersen, B.P., and Nissen, P. (2011). Crystal structure of a copper-transporting PIB-type ATPase. *Nature* 475, 59-64.

Hua, S., Inesi, G., and Toyoshima, C. (2000). Distinct topologies of mono- and decavanadate binding and photo-oxidative cleavage in the sarcoplasmic reticulum ATPase. *J. Biol. Chem.* 275, 30546-30550.

Kabsch, w. (1993). Automatic processing of rotation diffraction data from crystals of initially unknown symmetry and cell constants. *J. Appl. Cryst.* 26, 795-800.

Laursen, M., Bubltz, M., Moncoq, K., Olesen, C., Moller, J.V., Young, H.S., Nissen, P., and Morth, J.P. (2009). Cyclopiazonic Acid Is Complexed to a Divalent Metal Ion When Bound to the Sarcoplasmic Reticulum Ca^{2+} -ATPase. *J. Biol. Chem.* 284, 13513-13518.

Lu, Z., Dunaway-Mariano, D., and Allen, K.N. (2008) The catalytic scaffold of the haloalkanoic acid dehalogenase enzyme superfamily acts as a mold for the trigonal bipyramidal transition state. *Proc. Natl. Acad. Sci. U. S. A.* 105, 5687-5692.

McCoy, A.J., Grosse-Kunstleve, R.W., Adams, P.D., Winn, M.D., Storoni, L.C., and Read, R.J. (2007). Phaser crystallographic software. *J. Appl. Crystallogr.* 40, 658-674.

McIntosh, D.B. (1998). The ATP binding sites of P-type transport ATPases: properties, structure, conformations, and mechanisms of energy coupling. *Adv. Mol. Cell Biol.* 23A, 33-99.

McIntosh, D.B., Clausen, J.D., Woolley, D.G., MacLennan, D.H., Vilsen, B., and Andersen, J.P. (2004) Roles of conserved P domain residues and Mg^{2+} in ATP binding in the ground state and Ca^{2+} -activated states of sarcoplasmic reticulum Ca^{2+} -ATPase. *J. Biol. Chem.* 279, 32515-32523.

McIntosh, D.B., Woolley, D.G., and Berman, M.C. (1992). 2',3'-O-(2,4,6-trinitrophenyl)-8-azido-AMP and -ATP photolabel Lys-492 at the active site of sarcoplasmic reticulum Ca^{2+} -ATPase. *J. Biol. Chem.* 267, 5301-5309.

Moncoq, K., Trieber, C.A., and Young, H.S. (2007). The molecular basis for cyclopiazonic acid inhibition of the sarcoplasmic reticulum calcium pump. *J. Biol. Chem.* 282, 9748-9757.

Morth, J.P., Pedersen, B.P., Toustrup-Jensen, M.S., Sorensen, T.L., Petersen, J., Andersen, J.P., Vilsen, B., and Nissen, P. (2007). Crystal structure of the sodium-potassium pump. *Nature* **450**, 1043-1049.

Olesen, C., Picard, M., Winther, A.M., Gyrupe, C., Morth, J.P., Oxvig, C., Moller, J.V., and Nissen, P. (2007). The structural basis of calcium transport by the calcium pump. *Nature* **450**, 1036-1042.

Olesen, C., Sorensen, T.L., Nielsen, R.C., Moller, J.V., and Nissen, P. (2004). Dephosphorylation of the calcium pump coupled to counterion occlusion. *Science* **306**, 2251-2255.

Pick, U. (1982). The interaction of vanadate ions with the Ca-ATPase from sarcoplasmic reticulum. *J. Biol. Chem.* **257**, 6111-6119.

Read, R. (1990). Structure-factor probabilities for related structures. *Acta Crystallog. A* **46**, 900-912.

Read, R.J., and Schierbeek, A.J. (1988). A phased translation function. *J. Appl. Crystallogr.* **21**, 490-495.

Shigekawa, M., and Dougherty, J.P. (1978). Reaction mechanism of Ca²⁺-dependent ATP hydrolysis by skeletal muscle sarcoplasmic reticulum in the absence of added alkali metal salts. II. Kinetic properties of the phosphoenzyme formed at the steady state in high Mg²⁺ and low Ca²⁺ concentrations. *J. Biol. Chem.* **253**, 1451-1457.

Shigekawa, M., and Pearl, L.J. (1976). Activation of calcium transport in skeletal muscle sarcoplasmic reticulum by monovalent cations. *J. Biol. Chem.* **251**, 6947-6952.

Shinoda, T., Ogawa, H., Cornelius, F., and Toyoshima, C. (2009) Crystal structure of the sodium-potassium pump at 2.4 Å resolution. *Nature* **459**: 446-450.

Sorensen, T.L., Clausen, J.D., Jensen, A.M., Vilsen, B., Moller, J.V., Andersen, J.P., and Nissen, P. (2004a). Localization of a K⁺-binding Site Involved in Dephosphorylation of the Sarcoplasmic Reticulum Ca²⁺-ATPase. *J. Biol. Chem.* **279**, 46355-46358.

Sorensen, T.L., Moller, J.V., and Nissen, P. (2004b). Phosphoryl Transfer and Calcium Ion Occlusion in the Calcium Pump. *Science* **304**, 1672-1675.

Stansfield, P.J., Goose, J.E., Caffrey, M., Carpenter, E.P., Parker, J.L., Newstead, S., and Sansom, M.S. (2015) MemProtMD: Automated Insertion of Membrane Protein Structures into Explicit Lipid Membranes. *Structure* **23**, 1350-1361.

Stokes, D.L., Delavoie, F., Rice, W.J., Champeil, P., McIntosh, D.B., and Lacapère, J.J. (2005) Structural studies of a stabilized phosphoenzyme intermediate of Ca²⁺-ATPase. *J. Biol. Chem.* **280**, 18063-18072.

Toyoshima, C., Nakasako, M., Nomura, H., and Ogawa, H. (2000). Crystal structure of the calcium pump of sarcoplasmic reticulum at 2.6 Å resolution. *Nature* 405, 647-655.

Toyoshima, C., and Nomura, H. (2002). Structural changes in the calcium pump accompanying the dissociation of calcium. *Nature* 418, 605-611.

Toyoshima, C., Nomura, H., and Tsuda, T. (2004). Lumenal gating mechanism revealed in calcium pump crystal structures with phosphate analogues. *Nature* 432, 361-368.

Toyoshima, C., Yonekura, S., Tsueda, J., and Iwasawa, S. (2011). Trinitrophenyl derivatives bind differently from parent adenine nucleotides to Ca²⁺-ATPase in the absence of Ca²⁺. *Proc. Natl. Acad. Sci. U. S. A.* 108, 1833-1838.

Winn, M.D., Ballard, C.C., Cowtan, K.D., Dodson, E.J., Emsley, P., Evans, P.R., Keegan, R.M., Krissinel, E.B., Leslie, A.G., McCoy, A., *et al.* (2011). Overview of the CCP4 suite and current developments. *Acta Crystallogr D Biol Crystallogr* 67, 235-242.

Zhang, P., Toyoshima, C., Yonekura, K., Green, N.M., and Stokes, D.L. (1998). Structure of the calcium pump from sarcoplasmic reticulum at 8-Å resolution. *Nature* 392, 835-839.

FIGURE LEGENDS

Figure 1. Ca^{2+} -ATPase Reaction Cycle and Overall Structure of the $\text{E2}\cdot\text{VO}_3^-$ ·Thapsigargin·TNP-AMPPCP State

(A) Simplified Ca^{2+} -transport cycle with emphasis on the dephosphorylation reaction sequence. *Boxed* MgF_x , VO_3^- , AlF_4^- , and BeF_3^- indicate reaction intermediates for which analogs can be stabilized by the respective metal-fluorides (Danko et al., 2004; Olesen et al., 2007; Olesen et al., 2004; Toyoshima et al., 2004) or orthovanadate (Dupont and Bennett, 1982; Pick, 1982). (B) Overall view of the $\text{E2}\cdot\text{VO}_3^-$ ·thapsigargin·TNP-AMPPCP structure. The nucleotide binding domain is shown as *red cartoon*, the actuator domain as *blue cartoon*, and the phosphorylation domain as *yellow cartoon*. We furthermore determined the structures of the $\text{E2}\cdot\text{VO}_3^-$ state in the absence of thapsigargin, as well as with TNP-ATP instead of TNP-AMPPCP (cf. **Tables S1 and S2**). These structures did not vary significantly from the structure displayed here, except with respect to the expected presence or absence of thapsigargin at its previously defined binding site in the transmembrane region (Toyoshima and Nomura, 2002), in accordance with the previous findings that thapsigargin binding leads to few adaptive changes in the protein structure (Olesen et al., 2007) and does not affect the rotational freedom of the cytoplasmic domains (Clausen et al., 2011). This structure figure and all others in the article were generated using PyMOL (The PyMOL Molecular Graphics System, Version 1.5.0.5, Schrödinger, LLC). See also **Figure S1** and **Tables S1 and S2**.

Figure 2. Details of the Catalytic Site in the $\text{E2}\cdot\text{VO}_3^-$ Structure and Comparison with the Catalytic Site in $\text{E2}\cdot\text{AlF}_4^-$

(A) Details of the vanadate-binding site in $\text{E2}\cdot\text{VO}_3^-$. A simulated annealing $F_o - aF_c$ map calculated with empty $\text{MgVO}_3\cdot 3\text{H}_2\text{O}$ binding site is shown as *green mesh* (contoured at $5.0\ \sigma$), and an anomalous difference map is shown as *orange mesh* (contoured at $12.0\ \sigma$). (B) Alignment of the catalytic site in $\text{E2}\cdot\text{VO}_3^-$ (*light-grey sticks*; magnesium and water as spheres in dark colors) with that

of $E2 \cdot AlF_4^-$ (*yellow sticks*; magnesium and water as spheres in bright colors; PDB 3N5K (Bublitz et al., 2013)). (C) Alignment of the catalytic site in $E2 \cdot VO_3^-$ (same view as in Panel B) with that of the vanadate complex of the hexose phosphate phosphatase BT4131 from *Bacteroides thetaiotaomicron* (*yellow sticks* labeled according to the amino acid numbering of the hexose phosphate phosphatase; magnesium and water as spheres in bright colors; PDB 2RBK (Lu et al., 2008)). See also **Figure S2**.

Figure 3. Details of the Chloride Binding Site in the $E2 \cdot VO_3^-$ Structure

The chloride ion is shown as a *grey sphere*. (A) A simulated annealing $F_o - aF_c$ map calculated with empty Cl^- binding site is shown as *green mesh* (contoured at 3.0σ) and an anomalous difference map is shown as *orange mesh* (contoured at 4.0σ). Possible bond interactions (with distances in Å) are indicated by *dotted lines*. (B) A $2mF_o - DF_c$ electron density map (contoured at 2.0σ) is shown as *blue mesh*. (B) Overview of the interaction network connecting the chloride site to the nucleotide binding site and the phosphorylation site.

Figure 4. Comparison of the nucleotide binding sites in the $E2 \cdot VO_3^- \cdot thapsigargin \cdot TNP \cdot AMPPCP$ (A) and $E2 \cdot BeF_3^- \cdot TNP \cdot AMPPCP$ (B) structures

Side chains are shown as *light-grey sticks* and nucleotides as *yellow sticks*. Simulated annealing $F_o - iF_c$ maps calculated with empty nucleotide binding sites are shown as *green mesh* (contoured at 3.0σ). See also **Figure S4**.

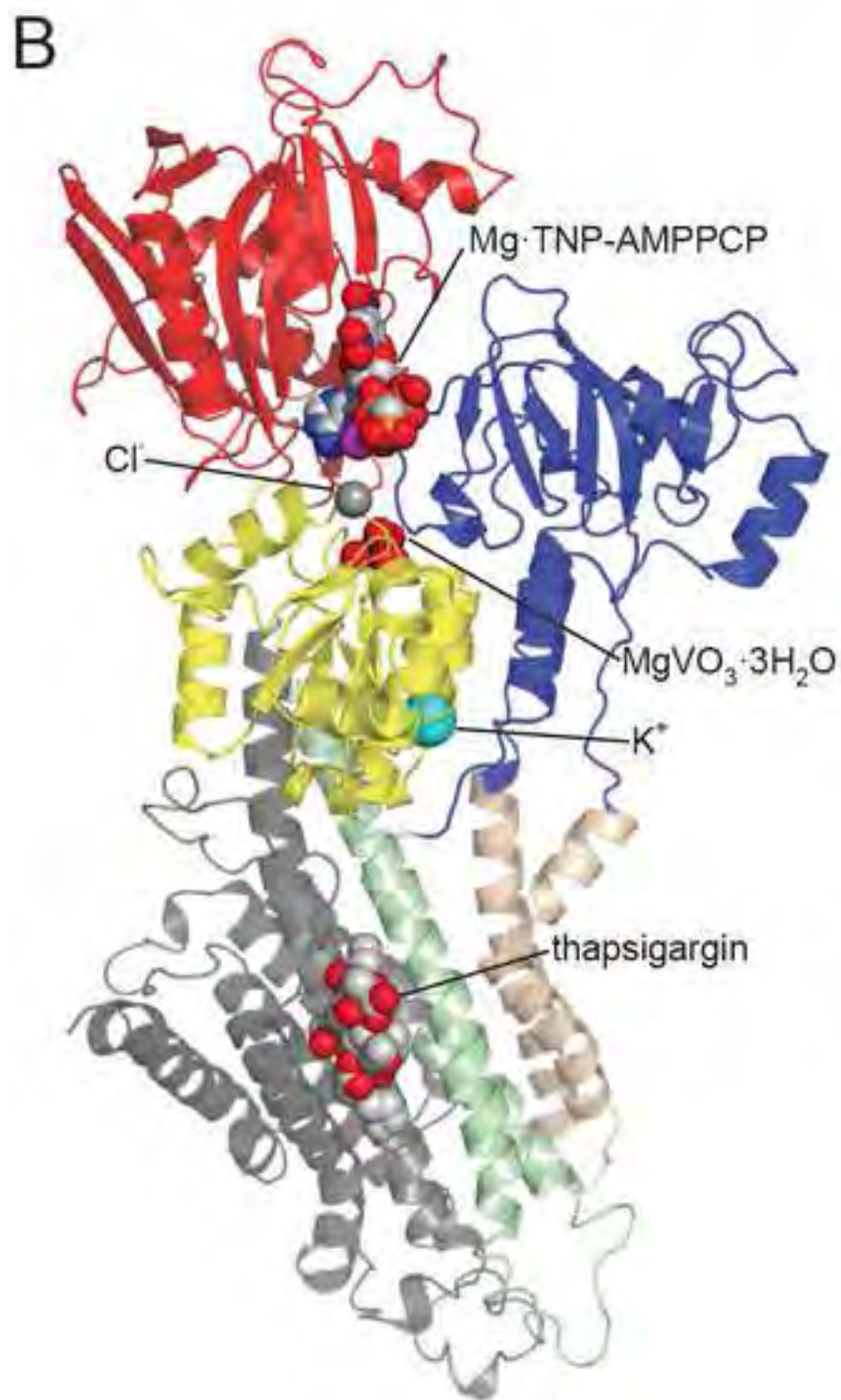
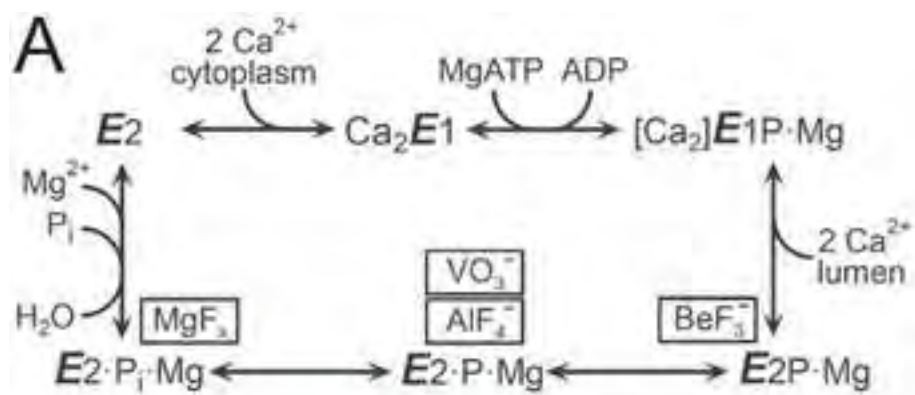
TABLES

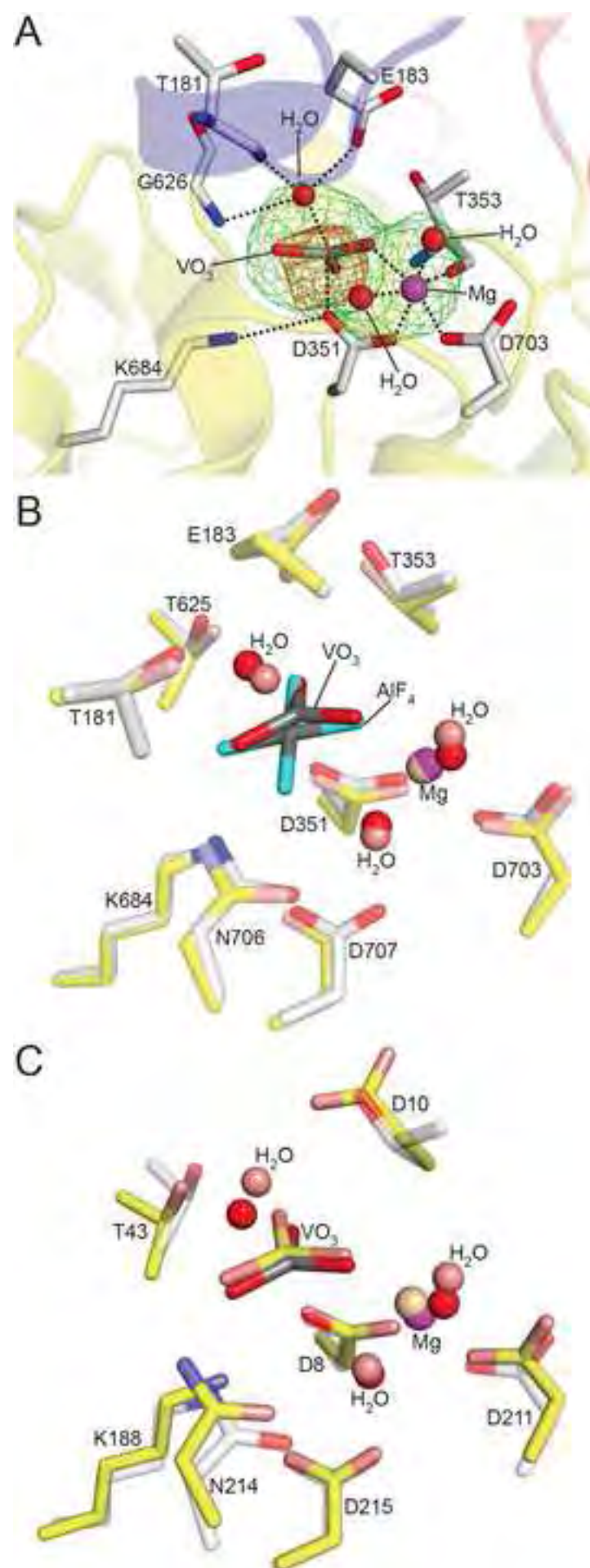
Table 1 Nucleotide affinity of the $E2 \cdot VO_3^-$ and $E2 \cdot BeF_3^-$ forms of the Ca^{2+} -ATPase. See also **Figure S3**.

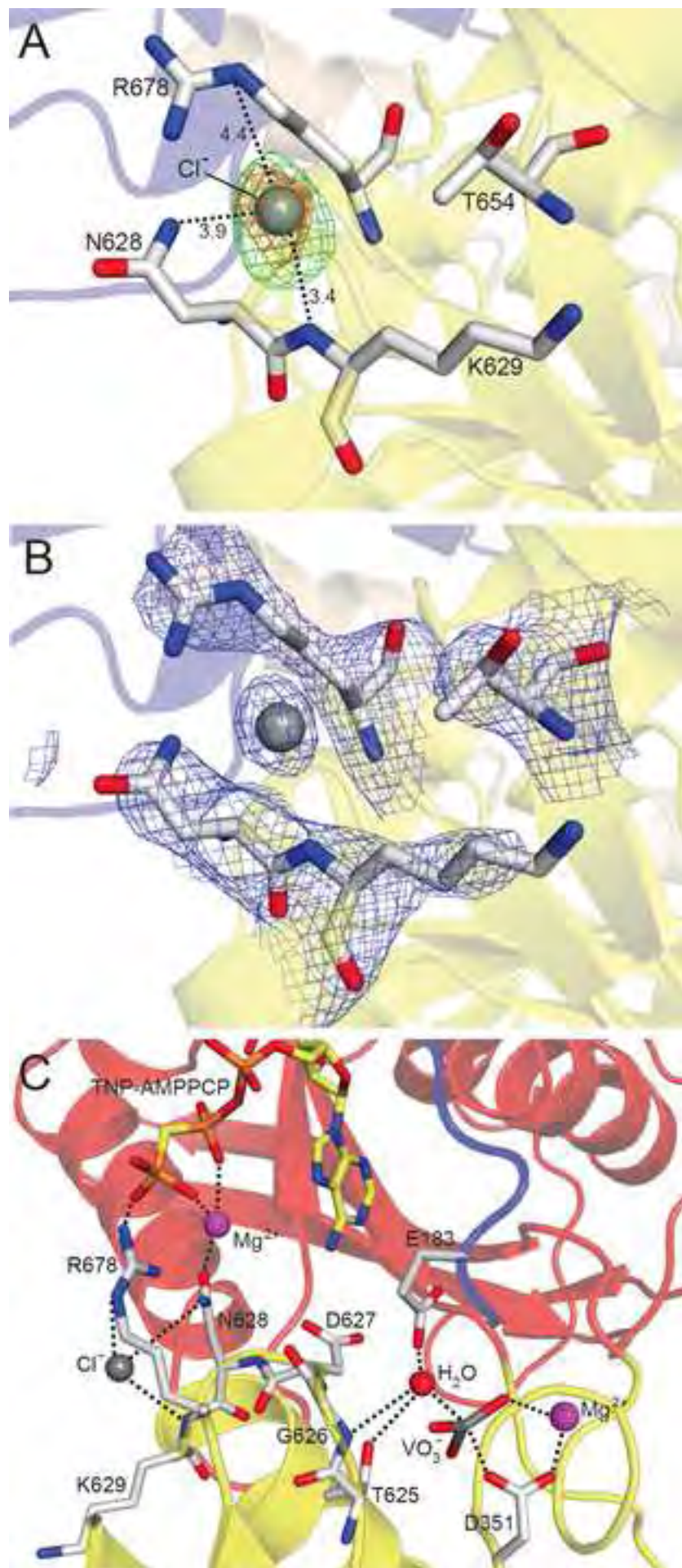
Nucleotide	$E2 \cdot VO_3^-$ ^a	$E2 \cdot BeF_3^-$ ^b
	K_D (nM)	
ATP	411 ± 15	2695 ± 110
AMPPCP	480 ± 15	4165 ± 229
ADP	9346 ± 1036	16785 ± 1676
TNP-ATP	2.1 ± 0.1	4.6 ± 0.2
TNP-AMPPCP	2.5 ± 0.1	16.7 ± 0.8
TNP-ADP	3.0 ± 0.2	25.9 ± 1.6

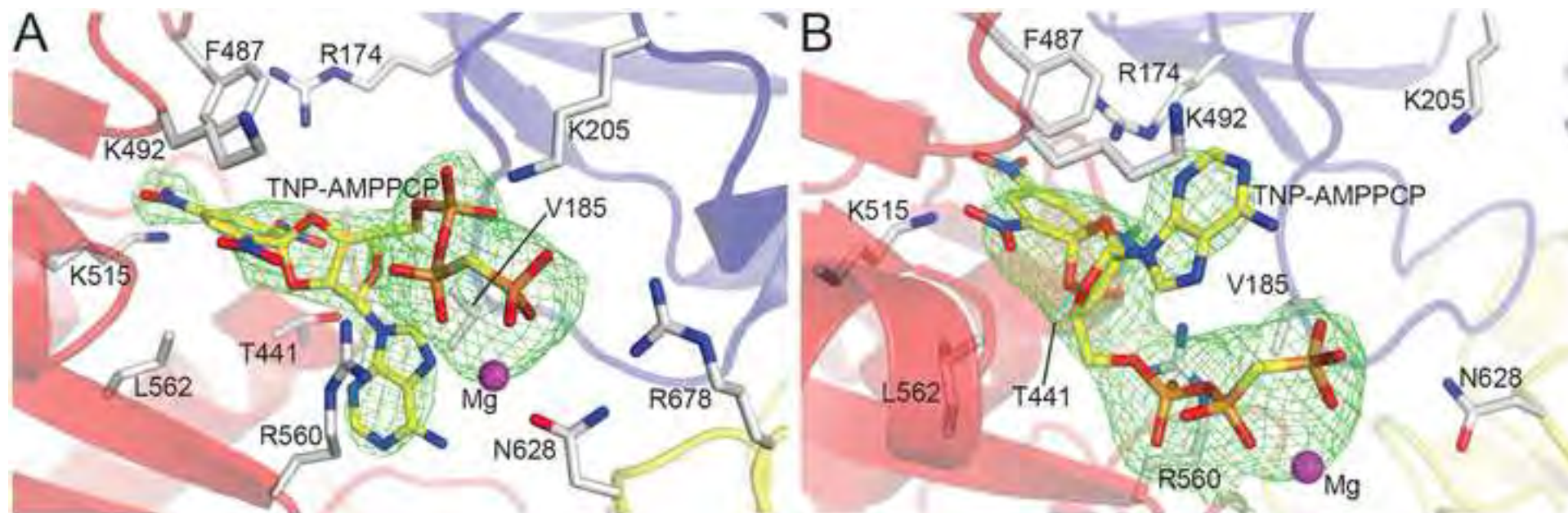
^a Corresponding to the data shown in **Figure S3A**.

^b Corresponding to the data shown in **Figure S3B**.









SUPPLEMENTAL DATA

Crystal Structure of the Vanadate-Inhibited Ca²⁺-ATPase

Johannes D. Clausen^{1,2,3,5,7}, Maike Bublitz^{1,2,6,7}, Bertrand Arnou^{1,2}, Claus Olesen^{1,2,3}, Jens Peter Andersen³, Jesper Vuust Møller^{2,3}, and Poul Nissen^{1,2,4}

¹Department of Molecular Biology and Genetics, ²Centre for Membrane Pumps in Cells and Disease – PUMPKIN, Danish National Research Foundation, ³Department of Biomedicine, and ⁴Danish Research Institute of Translational Neuroscience – DANDRITE, Nordic EMBL Partnership for Molecular Medicine.

Aarhus University, Aarhus, Denmark

⁵Present address: Pcovery ApS, Ole Maaløes Vej 3, Copenhagen, Denmark.

⁶Present address: Department of Biochemistry, University of Oxford, Oxford OX1 3QU, United Kingdom.

⁷These authors contributed equally to this work.

Correspondence should be addressed to P.N. (pn@mbg.au.dk).

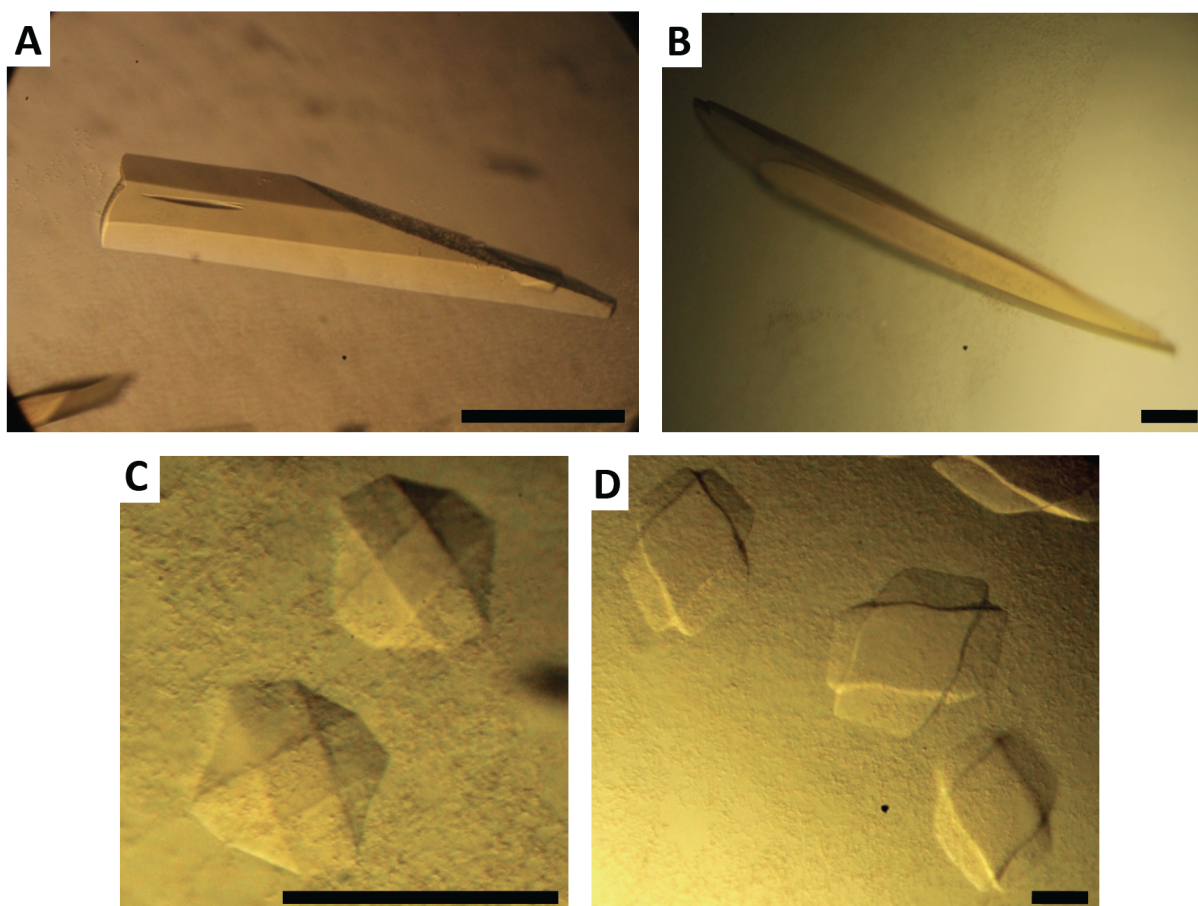


Figure S1. Crystals of the Ca^{2+} -ATPase in the $\text{E2}\cdot\text{VO}_3^-$ State (Related to Figure 1B)

The crystallization trials of the Ca^{2+} -ATPase accumulated in the $\text{E2}\cdot\text{VO}_3^-$ state gave rise to three distinct types of crystals, referred to here as type I (A), type II (B), and type III (C and D). The type I crystals grew in buffers containing high concentrations of Mg^{2+} (see **Tables S1 and S2**) and displayed a rectangular stick-like morphology. They grew to a typical length of ~ 0.3 mm, and diffraction data collected from these crystals invariably processed to space group P2_1 . The type II crystals grew under the same buffer conditions as the type I crystals (in fact, both crystal types were often present in the same drops), but were generally larger (up to 1 mm in length), with an irregular morphology, and diffraction data collected from these crystals invariably processed to space group $\text{P2}_1\text{2}_1\text{2}$. The type III crystals (shown here at day 1 (C) and day 7 (D) after crystallization drop set-up) grew in crystallization buffers devoid of Mg^{2+} . Diffraction data from the type III crystals processed to space group $\text{P2}_1\text{2}_1\text{2}$, with the same unit cell parameters as obtained with the type II crystals (**Tables S1 and S2**). In the absence of thapsigargin, only type I crystals grew, whereas the production of all three crystal types was feasible in the presence of thapsigargin. Furthermore, all three crystal types could be prepared with either TNP-ATP or TNP-AMPPCP as co-crystallizing nucleotide, whereas no crystals grew in the absence of nucleotide, or when AMPPCP or TNP-ADP were applied instead. The refined structures derived from the diffraction data obtained with the three crystal types displayed little variance, except with respect to the expected presence or absence of thapsigargin at its previously defined binding site in the transmembrane region (Toyoshima and Nomura, 2002). The black bar in the lower right corner of each panel represents ~ 0.1 mm.

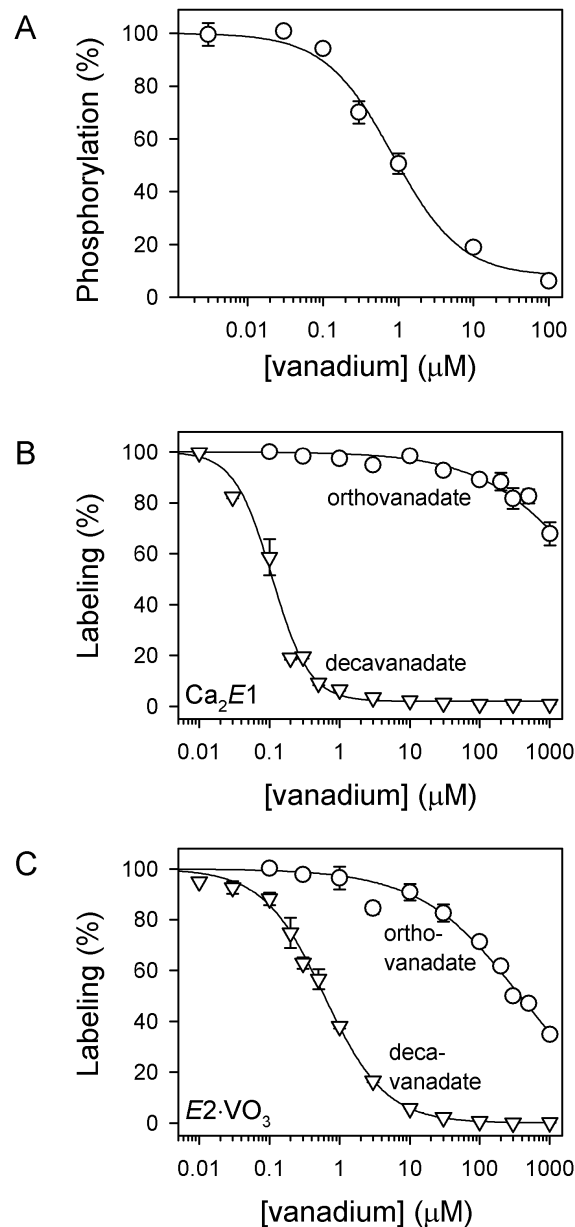


Figure S2. Binding of Orthovanadate and Decavanadate to the Ca^{2+} -ATPase (Related to Figure 2)

(A) Affinity of the E2 state of the Ca^{2+} -ATPase for orthovanadate determined by inhibition of the ability to undergo the $\text{E2} \rightarrow \text{Ca}_2\text{E1}$ transition and subsequently be phosphorylated by $[\gamma\text{-}^{32}\text{P}]\text{ATP}$. 1.6 pmol of Ca^{2+} -ATPase in non-solubilized sarcoplasmic reticulum vesicles was incubated for 30 min at 25°C , followed by 10 min at 0°C , in 80 μl of a buffer containing 40 mM MOPS/Tris (pH 7.0), 80 mM KCl, 2 mM EGTA, and 5 mM MgCl_2 with varying concentrations of a solution enriched in orthovanadate, as indicated on the *abscissa* (in total vanadium concentration, which likely varies from the true orthovanadate concentration, as discussed below). The degree of inhibition was determined by addition of CaCl_2 to a final concentration of 2.5 mM (giving a free Ca^{2+} concentration of 0.5 mM) and subsequent phosphorylation for 10 s at 0°C with 5 μM $[\gamma\text{-}^{32}\text{P}]\text{ATP}$. The reaction was stopped by acid quenching followed by acid SDS-polyacrylamide gel electrophoresis and quantification of the radioactivity associated with the Ca^{2+} -ATPase band, using previously established procedures (Vilsen et al., 1989). The level of phosphoenzyme obtained in the absence of vanadate was taken as 100%. The *line* shows the best fits of the Hill equation for inhibition (see **Experimental**

Procedures) to the data, giving a $K_{0.5}$ value of $0.84 \pm 0.13 \mu\text{M}$ and a Hill coefficient of 0.96 ($n = 3$, 24 data points). (**B** and **C**) Competitive inhibition of $[\gamma\text{-}^{32}\text{P}]\text{TNP-8N}_3\text{-ATP}$ photolabeling of $\text{Ca}^{2+}\text{-ATPase}$ accumulated in the $\text{Ca}_2\text{E1}$ state (**B**) or in the $\text{E2}\cdot\text{VO}_3^-$ state (**C**) by solutions enriched in either orthovanadate (*circles*) or decavanadate (*triangles*). The level of labeling obtained without adding the respective vanadate-solutions to the labeling mix was taken as 100%. The *lines* show the best fits of the Hill equation for inhibition to the data, giving the following K_D values (calculated using the equation for competitive inhibition, see **Experimental Procedures**): $\text{Ca}_2\text{E1}$, orthovanadate-enriched solution, $>1000 \mu\text{M}$ ($n = 2$, 40 data points); $\text{Ca}_2\text{E1}$, decavanadate-enriched solution, $0.027 \pm 0.002 \mu\text{M}$ ($n = 2$, 40 data points); $\text{E2}\cdot\text{VO}_3^-$, orthovanadate-enriched solution, $\sim 400 \mu\text{M}$ ($n = 2$, 40 data points); $\text{E2}\cdot\text{VO}_3^-$, decavanadate-enriched solution, $0.151 \pm 0.009 \mu\text{M}$ ($n = 2$, 40 data points).

The $[\gamma\text{-}^{32}\text{P}]\text{TNP-8N}_3\text{-ATP}$ photolabeling experiments demonstrate that decavanadate competes with nucleotide for binding, whereas the orthovanadate-enriched solution is much less effective in this respect. The K_D values measured for the competitive inhibition of labeling must be interpreted in light of the fact, that the vanadate solutions enriched in either orthovanadate or decavanadate are not necessarily homogenous with respect to these two vanadate species. Hence, ^{51}V NMR analysis has shown that the vanadium in the orthovanadate-enriched stock solution is made up by 70% orthovanadate and 30% pyrovanadate, whereas the decavanadate-enriched stock solution is very homogenous (when freshly made), containing no other vanadate species than decavanadate at detectable levels (Aureliano and Madeira, 1994). Dilution of the orthovanadate-enriched stock solution into buffer at neutral pH leads to the appearance of several other vanadate species, including tetrameric and pentameric vanadate, with the orthovanadate species now making up 33-46% of the total vanadium (Aureliano, 2000; Aureliano and Madeira, 1994). Upon dilution of the decavanadate-solution into pH 7.4 buffer, the decavanadate is partly converted to orthovanadate, albeit very slowly, displaying a $t_{1/2}$ in the order of hundreds of hours at 2°C (Aureliano and Madeira, 1994; Csermely et al., 1985). Given that the total incubation time with the decavanadate solution in the $[\gamma\text{-}^{32}\text{P}]\text{TNP-8N}_3\text{-ATP}$ labeling experiments shown here was less than 2 min, it can be assumed that all but traces of the added vanadium was present as the decameric species. The true affinity constants for the competitive inhibition by decavanadate are, thus, 10-fold lower than the measured K_D values, giving affinity constants for the binding of decavanadate to $\text{Ca}_2\text{E1}$ and $\text{E2}\cdot\text{VO}_3^-$ of 2.7 and 15 nM, respectively. The interpretation of the “orthovanadate”-dependence of photolabeling is more complex, given that the orthovanadate-enriched solution used was not homogenous, as argued above. The inhibition of labeling seen at high vanadium concentrations likely reflects the binding of (unspecified) vanadate oligomers to the nucleotide binding site.

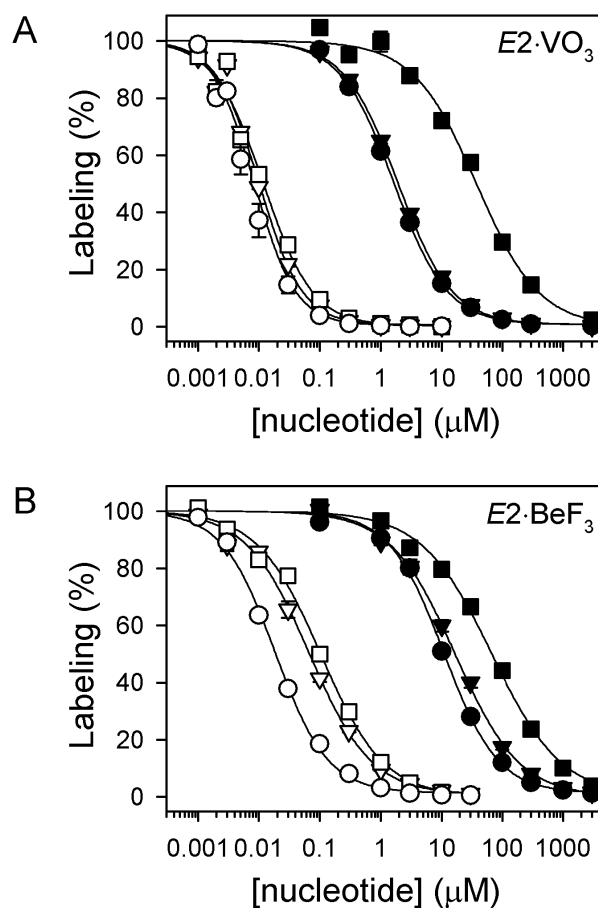


Figure S3. Nucleotide Affinity of the $E2\cdot\text{VO}_3^-$ and $E2\cdot\text{BeF}_3^-$ States of the $\text{Ca}^{2+}\text{-ATPase}$ (related to Table 1)

Competitive inhibition by ATP (closed circles), AMPPCP (closed triangles), ADP (closed squares), TNP-ATP (open circles), TNP-AMPPCP (open triangles), and TNP-ADP (open squares) of $[\gamma\text{-}^{32}\text{P}]\text{TNP-8N}_3\text{-ATP}$ photolabeling of $\text{Ca}^{2+}\text{-ATPase}$ accumulated in the $E2\cdot\text{VO}_3^-$ state (A) or in the $E2\cdot\text{BeF}_3^-$ state (B). In each case, the level of labeling obtained at [nucleotide] = 0 μM was taken as 100%. The lines show the best fits of the Hill equation for inhibition to the data, giving the K_D values (calculated using the equation for competitive inhibition, see **Experimental Procedures**) listed in **Table 1** (in all cases, $n = 2$, 40 data points).

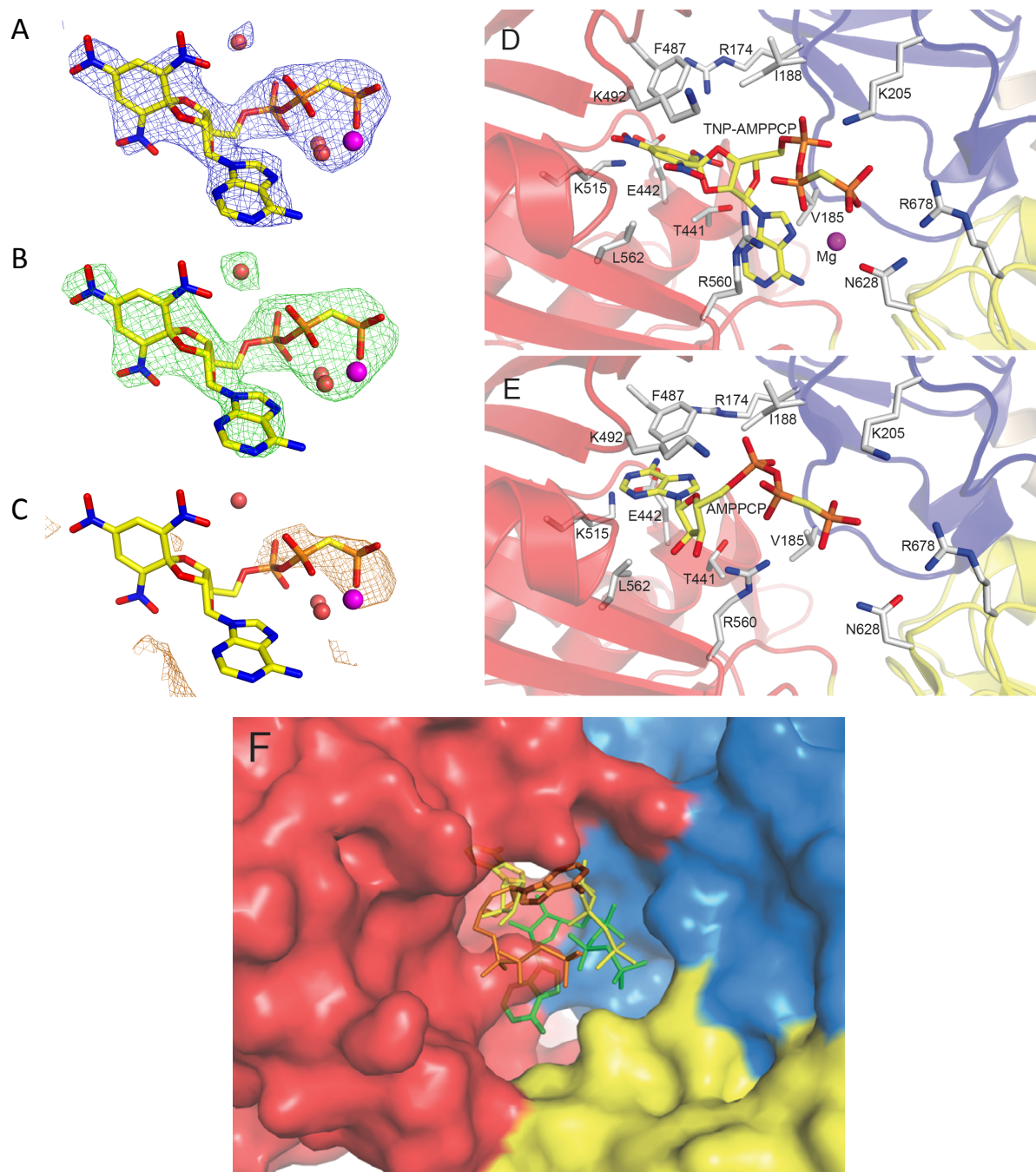


Figure S4. Details of the Nucleotide Binding Site in $E2 \cdot VO_3^-$ and Comparison with the $E2 \cdot AlF_4^-$ and $E2 \cdot BeF_3^-$ Structures (Related to Figure 4)

(A-C) Electron density maps at the nucleotide binding site in the $E2 \cdot VO_3^-$ ·thapsigargin·TNP-AMPPCP structure. TNP-AMPPCP is shown in stick model and a Mg^{2+} ion and three water molecules are shown as *magenta* and *red spheres*, respectively. A $2F_o - F_c$ map is shown in *blue mesh* contoured at 1.5σ (A), a simulated annealing $F_o - F_c$ map calculated without ligands is shown in *green mesh* contoured at 3.0σ (B), and an anomalous difference map is shown in *orange mesh* contoured at 2.5σ (C). (D-E) Structural Comparison of the Binding Sites for TNP-AMPPCP in the $E2 \cdot VO_3^-$ State and for AMPPCP in the $E2 \cdot AlF_4^-$ State. The structures shown are (D)

$E2 \cdot VO_3^-$ ·thapsigargin·TNP-AMPPCP (present work) and **(E)** $E2 \cdot AlF_4^-$ ·AMPPCP (PDB 3B9R (Olesen et al., 2007)). For both structures, the N domain is shown in *red cartoon*, the A domain in *blue cartoon*, the P domain in *yellow cartoon*, and the nucleotides and relevant side chains in *stick model*. The comparison illustrates the high homology of the arrangement of the side chains at the TNP-AMPPCP binding site in $E2 \cdot VO_3^-$ and the AMPPCP binding site in $E2 \cdot AlF_4^-$, suggesting that the TNP-nucleotides fit well into the natural preformed nucleotide-binding site in the $E2 \cdot P$ transition state. **(F)** Comparison of the position of the TNP-nucleotides in the $E2 \cdot VO_3^-$ and $E2 \cdot BeF_3^-$ states with that of AMPPCP in the $E2 \cdot AlF_4^-$ state. The structure shown is $E2 \cdot AlF_4^-$ ·AMPPCP (PDB 3B9R (Olesen et al., 2007)), with surface representations of the A-, P-, and N-domains (*yellow*, *blue*, and *red*, respectively). The nucleotide binding domains of the $E2 \cdot VO_3^-$ ·thapsigargin·TNP-AMPPCP and $E2 \cdot BeF_3^-$ ·TNP-AMPPCP structures (present work) were aligned with that of $E2 \cdot AlF_4^-$ ·AMPPCP. For clarity, the TNP moieties have been omitted and the nucleotides are single-colored (*yellow*, $E2 \cdot AlF_4^-$; *green*, $E2 \cdot VO_3^-$; *orange*, $E2 \cdot BeF_3^-$), with adenine nitrogen atoms indicated in darker tones of the respective color. The comparison illustrates the high degree of variability in the position of the nucleotides in the three structures and may delineate the pathways of entry/exit of nucleotide from the site.

Table S1. Data Collection and Refinement Statistics for the Structures Obtained by Co-Crystallization with TNP-AMPPCP (Related to Figure 1B)

Enzyme state	$E2\cdot VO_3^-$ -thapsigargin	$E2\cdot VO_3^-$ -thapsigargin	$E2\cdot VO_3^-$ -thapsigargin	$E2\cdot BeF_3^-$
Crystallization				
Crystallization buffer salt	MgCl ₂ ^c	MgCl ₂ ^d	NaCl ^e	MgCl ₂ ^f
Crystal morphology ^b	Type I	Type II	Type III	plate
Data collection				
No. data sets collected ^g	18	8	4	4
Space group	P2 ₁	P2 ₁ 2 ₁ 2	P2 ₁ 2 ₁ 2	P2 ₁ 2 ₁ 2 ₁
Unit cell	$a=130.1\text{ \AA}$	$a=86.4\text{ \AA}$	$a=86.8\text{ \AA}$	$a=57.5\text{ \AA}$
Dimensions	$b=94.6\text{ \AA}$	$b=118.8\text{ \AA}$	$b=118.4\text{ \AA}$	$b=115.0\text{ \AA}$
	$c=134.8\text{ \AA}$	$c=141.8\text{ \AA}$	$c=140.6\text{ \AA}$	$c=227.7\text{ \AA}$
	$\beta=107.1^\circ$	$\alpha=\beta=\gamma=90^\circ$	$\alpha=\beta=\gamma=90^\circ$	$\alpha=\beta=\gamma=90^\circ$
Resolution (\AA) ^a	128.9-3.40 (3.53-3.40)	141.8-3.05 (3.24-3.05)	140.6-3.10 (3.31-3.10)	80.9-3.05 (3.24-3.05)
Unique reflections ^a	43,130 (4,526)	28,547 (4,524)	26,958 (4,789)	29,573 (4,704)
I/σ ^a	10.1 (2.1)	13.0 (2.3)	11.6 (2.5)	12.4 (2.1)
CC (1/2) ^a	99.9 (74.0)	99.9 (75.6)	99.7 (81.5)	99.8 (85.5)
R_{meas} ^a	10.8 (78.3)	12.6 (95.1)	16.3 (92.2)	14.5 (112.6)
R_{pim} ^a	5.8 (41.8)	4.7 (34.7)	5.4 (29.5)	5.3 (40.6)
Completeness (%) ^a	99.4 (99.5)	100 (100)	99.9 (100.0)	100 (100)
Redundancy ^a	3.4 (3.4)	7.3 (7.5)	9.2 (9.4)	7.1 (7.5)
Refinement				
Resolution (\AA) ^a	76.3-3.40 (3.66-3.40)	73.8-3.05 (3.16-3.05)	70.3-3.10 (3.21-3.10)	57.5-3.05 (3.15-3.05)
No. reflections ^a	43,061 (8,562)	28,497 (2,785)	26,910 (2,665)	29,584 (2,614)
R_{work}/R_{free} (%) ^a	21.6/25.4 (28.9/33.4)	19.5/26.2 (27.1/31.0)	20.5/25.8 (29.1/37.2)	20.7/25.6 (30.7/39.2)
No. atoms				
Protein	15,342	7,671	7,671	7,671
Mg ²⁺ /K ⁺ /Cl ⁻	4/2/2	2/1/1	1/1/1	3/1/-
VO ₃ ⁻ /BeF ₃ ⁻	8/-	4/-	4/-	-/4
TNP-AMPPCP	92	46	46	46
Thapsigargin	92	46	46	-
Water	6	8	3	7
Avg. B-factors ^h				
N-/P-/A-domain	115.2/105.6/98.8	85.3/70.4/66.5	92.2/72.9/71.9	76.4/78.6/99.6
TM-domain	195.3	164.8	161.8	122.6
Mg ²⁺ /K ⁺ /Cl ⁻	96.6/116.1/99.3	57.8/72.1/60.4	58.8/86.8/99.8	166.9/130.6/-
VO ₃ ⁻ /BeF ₃ ⁻	83.7/-	56.4/-	67.0/-	-/66.0
TNP-AMPPCP	132.1	102.1	185.6	109.6
Thapsigargin	175.9	149.6	137.8	-
Water	94.7	57.2	50.2	87.7
R.m.s. deviations				
Bond lengths (\AA)	0.007	0.009	0.003	0.005
Bond angles ($^\circ$)	0.94	0.95	0.71	0.63

^a Numbers in parentheses refer to the highest resolution shells as indicated

^b See **Figure S1** for details on the various $E2\cdot VO_3^-$ crystal morphologies.

^c Crystallization buffer: 19.5% (w/v) PEG2000-MME, 11% (v/v) glycerol, 100 mM MgCl₂, 3% (v/v) *t*-butanol. The crystallization drop was equilibrated at 19 °C, and the crystal was flash cooled 13 days after set-up.

^d Crystallization buffer: 19.5% (w/v) PEG2000-MME, 11% (v/v) glycerol, 100 mM MgCl₂, 3% (v/v) *t*-butanol. The crystallization drop was equilibrated at 19 °C, and the crystal was flash cooled 13 days after set-up.

^e Crystallization buffer: 20% (w/v) PEG2000-MME, 12% (v/v) glycerol, 100 mM NaCl, 6% (v/v) 2-methyl-2,4-pentanediol. The crystallization drop was equilibrated at 19 °C, and the crystal was flash cooled 13 days after set-up.

^f Crystallization buffer: 37% (w/v) PEG400, 25 mM MgCl₂, and 50 mM glycine. The crystallization drop was equilibrated at 12 °C, and the crystal was flash cooled 6 days after set-up.

^g Data sets processed to a resolution of 4.0 Å or better are included.

^h High B-factor values after refinement are a common phenomenon in low-medium resolution structures. The average B-factor distribution of membrane protein structures (retrieved from MemProtMD (Stansfeld et al, 2015)) compared to general structures (retrieved from www.pdb.org) at 3.0 – 3.5 Å resolution is shifted to higher average atomic B-factors. The values observed here are well within the normal range observed. The effect is probably due to primarily poor bulk solvent models for crystals containing lipid/detergent micelles.

Table S2. Data Collection and Refinement Statistics for the Structures Obtained by Co-Crystallization with TNP-ATP (Related to Figure 1B)

Enzyme state	$E2 \cdot VO_3^-$	$E2 \cdot VO_3^- \cdot \text{thapsigargin}$	$E2 \cdot VO_3^- \cdot \text{thapsigargin}$
Crystallization			
Crystallization buffer salt	NaCl ^c	MgCl ₂ ^d	NaCl ^e
Crystal morphology ^b	Type I	Type I	Type III
Data collection			
No. data sets collected ^f	3	6	3
Space group	P2 ₁	P2 ₁	P2 ₁ 2 ₁ 2
Unit cell	$a=130.0 \text{ \AA}$	$a=130.6 \text{ \AA}$	$a=88.0 \text{ \AA}$
Dimensions	$b=95.1 \text{ \AA}$	$b=93.8 \text{ \AA}$	$b=120.6 \text{ \AA}$
	$c=135.5 \text{ \AA}$	$c=135.7 \text{ \AA}$	$c=142.0 \text{ \AA}$
	$\beta=107.2^\circ$	$\beta=107.3^\circ$	$\alpha=\beta=\gamma=90^\circ$
Resolution (\AA) ^a	47.6-3.40 (3.53-3.40)	93.8-3.30 (3.42-3.30)	47.3-3.45 (3.78-3.45)
Unique reflections ^a	43,662 (4,558)	47,392 (4,621)	20,545 (4,805)
I/σ ^a	10.6 (1.8)	12.5 (2.1)	14.2 (2.8)
CC (1/2) ^a	99.6 (59.6)	99.8 (75.5)	99.8 (86.5)
R_{meas} ^a	14.8 (104.5)	11.1 (94.9)	15.6 (123.9)
R_{pim} ^a	7.6 (53.4)	4.6 (39.8)	4.4 (34.4)
Completeness (%) ^a	99.8 (99.8)	99.9 (99.9)	100 (100)
Redundancy ^a	3.7 (3.8)	5.7 (5.5)	12.8 (12.9)
Refinement			
Resolution (\AA) ^a	45.1-3.40 (3.66-3.40)	78.9-3.30 (3.51-3.30)	47.3-3.45 (3.63-3.45)
No. reflections ^a	43,601 (8,679)	47,351 (7,840)	20,463 (2,862)
R_{work}/R_{free} (%) ^a	20.9/25.7 (29.2/37.3)	19.7/23.0 (26.9/33.1)	23.0/27.7 (32.9/34.5)
No. atoms			
Protein	15,342	15,342	7,671
Mg ²⁺ /K ⁺ /Cl ⁻	2/2/-	4/2/2	1/1/-
VO ₃ ⁻	8	8	4
TNP-ATP	92	92	46
Thapsigargin	-	92	46
Water	6	8	3
Avg. B-factors ^g			
N-/P-/A-domain	106.7/95.9/92.9	103.0/94.1/87.3	131.8/99.2/98.2
TM-domain	207.0	176.1	228.3
Mg ²⁺ /K ⁺ /Cl ⁻	73.3/120.3/-	116.7/102.9/81.3	133.4/115.3/-
VO ₃ ⁻	80.8	93.5	90.7
TNP-ATP	176.4	158.9	245.8
Thapsigargin	-	183.3	190.2
Water	87.3	99.0	118.8
R.m.s. deviations			
Bond lengths (\AA)	0.005	0.004	0.004
Bond angles ($^\circ$)	0.78	0.91	0.71

^a Numbers in parentheses refer to the highest resolution shells as indicated

^b See **Figure S1** for details on the various $E2 \cdot VO_3^-$ crystal morphologies.

^c Crystallization buffer: 22% (w/v) PEG2000-MME, 9% (v/v) glycerol, 100 mM NaCl, 3% (v/v) *t*-butanol. The crystallization drop was equilibrated at 19 °C, and the crystal was flash cooled 3 days after set-up.

^d Crystallization buffer: 19% (w/v) PEG2000-MME, 11% (v/v) glycerol, 100 mM MgCl₂, 3% (v/v) *t*-butanol. The crystallization drop was equilibrated at 19 °C, and the crystal was flash cooled 9 days after set-up.

^e Crystallization buffer: 21% (w/v) PEG2000-MME, 10% (v/v) glycerol, 100 mM NaCl, 6% (v/v) 2-methyl-2,4-pentanediol. The crystallization drop was equilibrated at 19 °C, and the crystal was flash cooled 5 days after set-up.

^f Data sets processed to a resolution of 4.0 \AA or better are included.

^g High B-factor values after refinement are a common phenomenon in low-medium resolution structures. The average B-factor distribution of membrane protein structures (retrieved from MemProtMD (Stansfeld et al, 2015)) compared to general structures (retrieved from www.pdb.org) at 3.0 – 3.5 \AA resolution is shifted to higher average atomic B-factors. The values observed here are well within the normal range generally observed. The effect is probably due to primarily poor bulk solvent models for crystals containing lipid/detergent micelles.

SUPPLEMENTAL EXPERIMENTAL PROCEDURES

Nucleotide Synthesis

TNP-ATP, TNP-AMPPCP, TNP-ADP, and TNP-8N₃-ATP were prepared similarly, by TNP-derivatization of the parent nucleotides, using a previously described procedure (Hiratsuka, 1982; McIntosh and Woolley, 1994) with modifications (Clausen et al., 2016). 13.5 mg 5,5'-dithiobis(2-nitro-benzoic acid) (Sigma-Aldrich) was dissolved in 500 μ l 0.8 M Na₂CO₃/NaHCO₂ (pH 9.5) at 37 °C and supplemented with 40 μ l 1 M 2,4,6-trinitrobenzenesulfonic acid (Sigma-Aldrich). 250 μ l of this solution was then added to 450 μ l of a 10 mM solution of either ATP, AMPPCP, ADP (Sigma-Aldrich), or 8N₃-ATP (BioLog Life Science Institute, Germany), followed by incubation in the dark for 4 h at 25 °C. The reaction was diluted into 12 ml deionized water and loaded onto a 0.5 \times 4 cm Whatman DE52 column (GE Healthcare) equilibrated with water. The column was washed with water and then developed with ammonium formate solutions (pH 8.2) as follows: 2 \times 5 ml 0.2 M, 3 \times 5 ml 0.5 M, and 5 \times 5 ml 1 M. The last 21 ml of the 1 M ammonium formate eluates were applied to a C₁₈ Sep-Pak solid-phase extraction cartridge (Waters). The cartridge was perfused with 2 ml 10 mM KH₂PO₄ (pH 7.0), followed by elution of the nucleotide with 2 ml 60% (v/v) acetonitrile. The organic solvent, as well as some of the water, was removed by blowing over the solution with nitrogen until the volume reached ~300 μ l with a nucleotide concentration of 3-5 mM.

Preparation of Vanadate Solutions

Stock solutions enriched in either orthovanadate or decavanadate were prepared according to previously established protocols (Ko et al., 1997; Varga et al., 1985). The orthovanadate stock solution (60 mM) was prepared by dissolving Na₃VO₄ in water, followed by adjustment of the pH to 10.0 with HCl (giving rise to the appearance of a strong yellow color, indicative of the presence of decavanadate). The solution was boiled for two minutes (whereby the solution became transparent), cooled on ice, and the pH readjusted to 10.0 with NaOH. The boiling, cooling, and pH adjustments were repeated twice, whereupon the pH remained stable at 10.0. The orthovanadate concentration was measured spectrophotometrically at 265 nm using the extinction coefficient of 2925 M⁻¹cm⁻¹. The decavanadate stock solution (20 mM) was prepared by dilution of 10 ml of the orthovanadate stock solution in 20 ml water, followed by adjustment of the pH to 2.0 with a few drops of 5 N HCl. The solution was left for some hours at 4°C for equilibration, followed by readjustment of the pH to 6.5 with NaOH. The orthovanadate and decavanadate stock solutions were stored at -80 and 4°C, respectively, until use.

Protein Preparation

Sarcoplasmic reticulum Ca²⁺-ATPase (SERCA1a isoform) was prepared from sarcoplasmic reticulum vesicles isolated from rabbit hind leg skeletal muscle. For the purpose of crystallization trials, the membranes were further extracted and purified with a low concentration of deoxycholate according to established procedures (Andersen et al., 1985). The membrane preparation was washed by centrifugation at 130,000g for 35 min and 4°C in 100 mM MOPS/Tris (pH 6.8) and 80 mM KCl, and the pellet was resuspended in 100 mM MOPS/Tris (pH 6.8), 80 mM KCl, 20% (v/v) glycerol, 1.5 mM EGTA, and 0.25-0.4 mM MgCl₂. The resuspended pellet was supplemented with either 1 mM orthovanadate-enriched solution or 0.5 mM BeSO₄ and 5 mM NaF, and either with or without 0.15 mM thapsigargin, followed by incubation for 1-2 h on ice. Nucleotide was added to give a final concentration of either 0.4 mM (for the TNP-derivatized nucleotides) or 1 mM (for AMPPCP), followed by incubation for 15-30 min on ice. Finally, the protein was solubilized by addition of octaethyleneglycol dodecylether (C₁₂E₈) at a detergent:protein ratio of 1.5:1 (w/w), incubated for 15-30 min on ice, and centrifuged at 130,000g for 35 min and 4°C. The supernatant, which had a protein content of ~10 mg/ml, was used directly for crystallization trials.

Protein Crystallization

Crystallization was carried out using the vapor diffusion technique in hanging crystallization drops (1-5 μ l) manually pipetted onto siliconized glass cover slides (Hampton Research) sealed to the reservoir with microscopy immersion oil. Each crystallization drop contained a mixture of the C₁₂E₈-solubilized Ca²⁺-ATPase solution and the crystallization buffer, typically in a 1:1 ratio, and was equilibrated against the reservoir containing 400 μ l of the crystallization buffer. Initial screening included crystallization buffers containing various concentrations of different polyethylene glycols, salts, organic solvents, and glycerol. Promising hits were then subjected to narrower grid screens. The crystallization buffers that gave rise to the crystals, from which the highest resolution X-ray diffraction data sets were obtained, are detailed in **Tables S1 and S2**. The crystals were mounted in either LithoLoops (Molecular Dimensions) or nylon CryoLoops (Hampton Research) before flash-cooling in liquid nitrogen.

Diffraction Data Collection

X-ray diffraction data were collected at the Deutsches Elektronen-Synchrotron DESY beamlines P13 and P14 (Hamburg, Germany), the Swiss Light Source beamline X06SA (Villigen, Switzerland), the Synchrotron SOLEIL beamline PROXIMA1 (Gif-sur-Yvette Cedex, France), the European Synchrotron Radiation Facility beamlines ID23-1 and ID23-2 (Grenoble, France), the Diamond Light Source beamline I24 (Oxfordshire, UK), and the MAX Laboratory beamline I911-2 (Lund, Sweden).

Competitive Inhibition of [γ -³²P]TNP-8N₃-ATP Photolabeling

The synthesis of the [γ -³²P]TNP-8N₃-ATP photolabel, its application as a specific photolabel of the Ca²⁺-ATPase, the competitive inhibition by various ligands (nucleotides and monomeric/polymeric vanadate species) of [γ -³²P]TNP-8N₃-ATP photolabeling, the quantification of ³²P-labeled bands by electronic autoradiography following SDS-PAGE, and the analysis of the results were carried out using previously established procedures (McIntosh et al., 1996; Seebregts and McIntosh, 1989) with modifications (Clausen et al., 2011; Clausen et al., 2016). The medium used for the photolabeling contained 25 mM EPPS/tetramethyl ammonium hydroxide (pH 8.5), 2 mM EDTA, 17.4% (v/v) glycerol, 1-5 nM Ca²⁺-ATPase, and [γ -³²P]TNP-8N₃-ATP without or with the ligand of interest at the concentrations indicated in the figures. The analysis of the data obtained from the inhibition of TNP-8N₃-ATP photolabeling was based on the Hill equation for inhibition, $Y = Y_{\max} \cdot (1 - [\text{Lig}]^h / (K_{0.5}^h + [\text{Lig}]^h))$, in which Y and Y_{\max} are the amount of photolabeled Ca²⁺-ATPase and the maximal value, respectively, $K_{0.5}$ is the concentration of ATP giving half-maximum effect, h is the Hill coefficient (varying between 0.72 and 1.42 in the nucleotide binding experiments), and $[\text{Lig}]$ is the concentration of the ligand of interest. The “true” dissociation constant, K_D , for ligand binding was calculated from the measured $K_{0.5}$ values using the validated equation for competitive inhibition (McIntosh et al., 1996).

SUPPLEMENTAL MODELING FILES

5a3q: Crystal structure of the (SR) Calcium ATPase E2-vanadate complex bound to thapsigargin and TNP-AMPPCP (see Fig. 1B and Table S1)

5a3r: Crystal structure of the (SR) Calcium ATPase E2.BeF₃⁻ complex bound to TNP-AMPPCP (see Fig. 4B and Table S1)

5a3s: Crystal structure of the (SR) Calcium ATPase E2-vanadate complex bound to thapsigargin and TNP-ATP (see Experimental procedures and Table S2)